Journal of Sound and Vibration 330 (2011) 2265–2280

Contents lists available at ScienceDirect

Journal of Sound and Vibration

journal homepage: www.elsevier.com/locate/jsvi

Imaging of directional distributed noise sources

D. Papamoschou

Department of Mechanical and Aerospace Engineering, University of California, Irvine, CA 92697, United States

ARTICLE INFO

Article history:
Received 9 August 2010
Accepted 23 November 2010
Handling Editor: P. Joseph
Available online 15 December 2010

ABSTRACT

This study relates to the acoustic imaging of noise sources that are distributed and strongly directional, such as in turbulent jets. The goal is to generate high-resolution noise source maps with self-consistency, i.e., their integration over the extent of the noise source region gives the far-field pressure auto-spectrum for a particular emission direction. Self-consistency is possible by including a directivity factor in the formulation of the source cross-spectral density. The resulting source distribution is based on the complex coherence, rather than the cross-spectrum, of the measured acoustic field. For jet noise, whose spectral nature changes with emission angle, it is necessary to conduct the measurements with a narrow-aperture array. Three coherence-based imaging methods were applied to a Mach 0.9 turbulent jet: delay-and-sum beamforming; deconvolution of the beamformer output; and direct spectral estimation that relies on minimizing the difference between the measured and modeled coherences of the acoustic field. The delay-and-sum beamforming generates noise source maps with strong spatial distortions and sidelobes. Deconvolution leads to a five-fold improvement in spatial resolution and significantly reduces the intensity of the sidelobes. The direct spectral estimation produces maps very similar to those obtained by deconvolution. The coherence-based noise source maps, obtained by deconvolution or direct spectral estimation, are similar at small and large observation angles relative to the jet axis.

1. Introduction

Noise source location is central to the understanding, modeling, and suppression of noise from aircraft. Microphone techniques have included acoustic mirrors [1,2], polar correlation [3–6], and phased arrays [7–13]. The theoretical foundation of noise source location using cross-correlations of multiple microphone signals was established by Billingsley and Kinns [7]. Frequency-domain approaches for processing the microphone array data were introduced by Gramann and Mocio [8], Mosher [9], and Humphreys et al. [10]. For the aforementioned noise source imaging methods, the output of the instrument is a convolution between a known kernel (the point spread function) and the noise source distribution. The noise source distribution has a presumed form, e.g., an array of monopoles. Recent studies by Brooks and Humphreys [14] and by Dougherty [15] have proposed methods of deconvolution.

Sound emission from turbulent jets issuing from engine exhausts is of paramount interest to aircraft noise. The jet noise source is extended, directional, and its spectral nature changes with emission angle. At low polar angles with respect to the downstream axis, the spectrum is peaky, indicating strong temporal coherence; at large angles, the spectrum is flatter, indicating weak temporal coherence. The transition is fairly distinct and the transition polar angle depends on the jet velocity. It is around 60° for a high-subsonic jet—the focus of the present study. The different spectral shapes have raised the

E-mail address: dpapamos@uci.edu

0022-460X/$ - see front matter
doi:10.1016/j.jsvi.2010.11.025

Nomenclature

a	ambient speed of sound
b	beam width, $V(x,x\pm b/2,\omega)=\frac{1}{2}V(x,x,\omega)$
D	jet diameter
f	cyclic frequency
G_{mn}	cross-spectrum matrix
I_{ML}	integral of main lobe of point spread function
$\mathcal{L}$	axial extent of noise source region
$\ell_m(x)$	distance of microphone m from source point x
K	number of discrete sources
M	number of microphones
R	array radius
$q(x,\theta,t)$	noise source strength
Sr	Strouhal number = fD/U
t	time
T_{mn}	array response matrix
U	jet velocity
$V(x,\xi,\omega)$	point spread function (PSF)
W_m, w_m	weight for microphone m
$\overline{w}_m$	dimensionless weight for microphone m
x,ξ	spatial coordinates
γ_{mn}	complex coherence
θ	polar angle from jet axis
Θ_{mn}	directivity matrix
λ	wavelength
μ_{mn}	angular response of polar array
$\Phi(x,\omega)$	array beamformer output
$\psi(x,\omega)$	coherence-based source distribution
$\Psi(x,\omega)$	spectrum-based source distribution
τ_m	time delay for microphone m
θ_m	polar angle of microphone m
θ_a	average array polar angle
ω	radian frequency = $2\pi f$

possibility of disparate noise source mechanisms, and distributions, for radiation at small and large angles [16,17]. To enable such differentiation, imaging of the noise sources should employ an array with narrow polar aperture. However, even within a reasonably small aperture, the sound pressure level spectrum changes significantly near the direction of peak emission. This is illustrated by Fig. 1, which plots sound pressure level spectra within a narrow range of polar angle for noise emitted at small and large angles from the jet axis. At low polar angle, the spectrum changes significantly within a few degrees, even though it retains its coherent nature. At large polar angles the directivity of the spectrum is weak.

The goal of the current work is development of a methodology for imaging extended and directional noise sources such that the resulting noise source maps are devoid to the extent possible of the array response and are self-consistent. Self-consistency here means that spatial integration of the noise source gives the far-field auto-spectrum in a particular polar direction. A further consideration, pertinent to jet noise, is allowing for the possibility that the noise source distribution is different at small and large polar angles. This necessitates an array with small polar aperture. Although several past studies have used microphone arrays to image jet noise [11–13], their apertures were too large to enable such differentiation, and self-consistency was not addressed in a systematic manner.

To achieve self-consistency it will be shown that directionality must be incorporated in the formulation of the noise source model. The resulting method is based on the complex coherence, rather than the cross-spectrum, of the pressure field. This idea represents an extension of concepts presented in the seminal paper on polar correlation technique by Fisher et al. [3] which was applied to model and full-scale jet noise data. The proposed methodology is inherently applicable to noise source maps that have been "cleaned" of the effects of the array response. We present two such methods to clean the noise source maps: deconvolution of the traditional delay-and-sum beamformer output and a direct spectral estimation method that

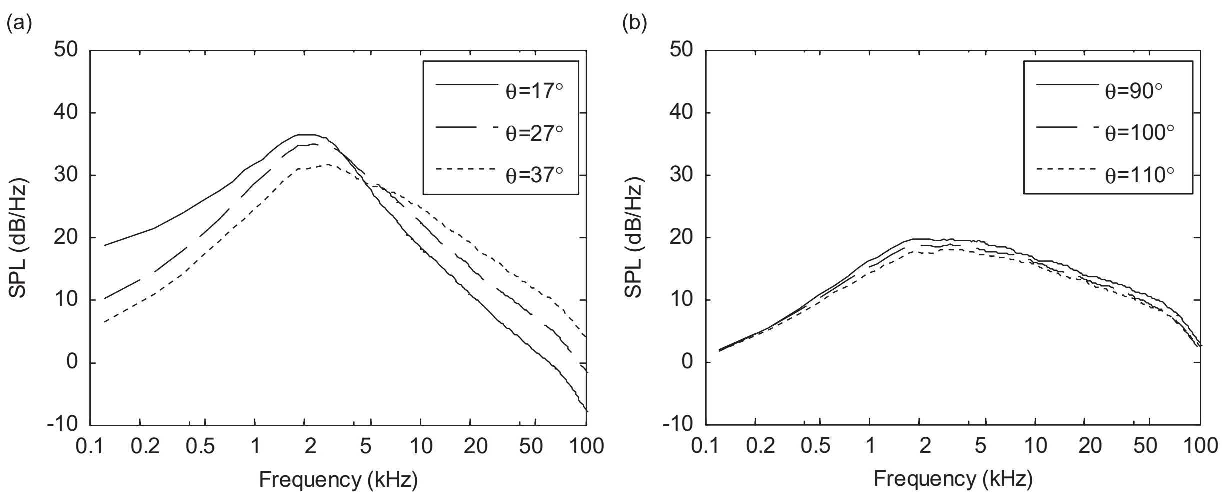

Fig. 1. Variation of spectrum with polar angle from jet axis for a Mach 0.9 cold jet. (a) Direction of peak emission; (b) broadside direction.

obviates delay-and-sum beamforming. Finally we comment on the measured polar coherence of the acoustic field and its proper interpretation.

2. Formulation of directional source distribution

Consistent with the general approach used in several past studies (e.g., [3,7,12]), the jet noise source is approximated by a one-dimensional distribution, along the jet axis x, of equivalent sources as viewed by a far-field observer. Fig. 2 illustrates the linear source model and the location of the sensing microphones. We denote the source distribution $q(x,\theta,t)$, with θ the polar angle measured from location x. Inclusion of the polar angle explicitly in the formulation of the noise source facilitates treatment of directive sources, as shown below. We assume an array aperture sufficiently small so that, for a fixed array location, all the microphones sense the same type of noise source q. However, we allow for the possibility that the distribution of q may be vary as the array moves from low to high polar angle, corresponding to the disparate spectra discussed in Introduction.

Considering the linear source model of Fig. 2 and assuming spherical spreading in a quiescent medium with uniform speed of sound a, the signal received by the mth microphone of the array is

$$p_m(t) = \int_{\mathcal{L}} \frac{1}{\ell_m(x)} q(x,\theta_m(x),t-\tau_m(x))\, \mathrm{d}x \tag{1}$$

where

$$\tau_m(x) = \frac{\ell_m(x)}{a} \tag{2}$$

is the retarded time from point x to microphone m. Integration is carried over the region of interest $\mathcal{L}$ where significant sound sources are expected. The Fourier transform of the microphone output is

$$P_m(\omega) = \int_{\mathcal{L}} \frac{1}{\ell_m(x)} \mathrm{e}^{-\mathrm{i}\omega\tau_m(x)} Q(x,\theta_m(x),\omega)\, \mathrm{d}x \tag{3}$$

where $Q(x,\theta,\omega)$ is the Fourier transform of $q(x,\theta,t)$. In frequency-domain microphone array methods, the central parameter is the cross-spectral matrix:

$$G_{mn}(\omega) \equiv \langle P_m^*(\omega) P_n(\omega) \rangle \tag{4}$$

where $\langle\ \rangle$ denotes time averaging. Substituting Eq. (3),

$$G_{mn}(\omega) = \int_{\mathcal{L}}\int_{\mathcal{L}} \frac{1}{\ell_m(x)\ell_n(\xi)} \mathrm{e}^{\mathrm{i}\omega[\tau_m(x)-\tau_n(\xi)]} \langle Q^*(x,\theta_m(x),\omega) Q(\xi,\theta_n(\xi),\omega) \rangle\ \mathrm{d}x\, \mathrm{d}\xi \tag{5}$$

The bracketed term is the cross-spectral density of the noise source and needs to be modeled. Here we assume a spatially incoherent source distribution and, for reasons that will become apparent shortly, introduce a *directivity matrix* $\Theta_{mn}(x,\xi,\omega)$ as follows:

$$\langle Q^*(x,\theta_m(x),\omega) Q(\xi,\theta_n(\xi),\omega) \rangle = \psi(x,\omega)\Theta_{mn}(x,\xi,\omega)\delta(x-\xi) \tag{6}$$

The function $\psi(x,\omega)$ represents a source distribution that is presumed independent of observation angle for a given position of the narrow-aperture array. As mentioned above, we allow for the possibility that $\psi(x,\omega)$ may be different at small and large

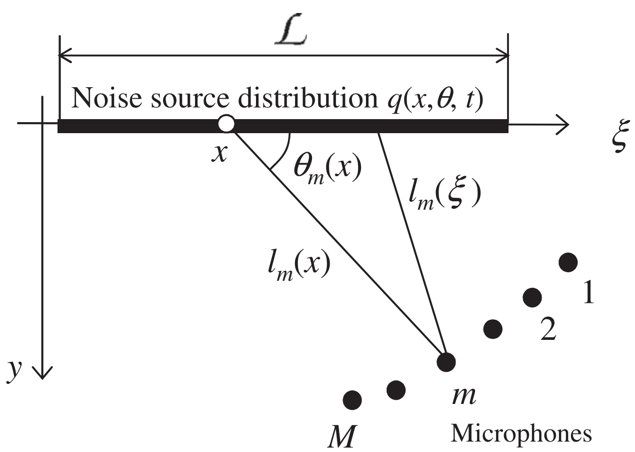

Fig. 2. Linear distribution of noise sources and microphone array.

polar angles of the array. Using Eq. (6), the cross-spectral matrix becomes

$$G_{mn}(\omega) = \int_{\mathcal{L}} \frac{1}{\ell_m(x)\ell_n(x)} \mathrm{e}^{\mathrm{i}\omega[\tau_m(x)-\tau_n(x)]} \psi(x,\omega)\Theta_{mn}(x,x,\omega)\,\mathrm{d}x \tag{7}$$

and its diagonal terms (auto-spectra) satisfy

$$G_{mm}(\omega) = \int_{\mathcal{L}} \frac{1}{\ell_m(x)^2} \psi(x,\omega)\Theta_{mm}(x,x,\omega)\,\mathrm{d}x \tag{8}$$

The necessity of including the directivity matrix $\Theta_{mn}(x,\xi,\omega)$ in the formulation of the source cross-spectral density of Eq. (6) is now evident. Without it, it would have been impossible for the right-hand side of Eq. (8) to match the directivity of the left-hand side as exemplified in Fig. 1. A convenient form for the directivity matrix is

$$\Theta_{mn}(x,\xi,\omega) = \sqrt{G_{mm}(\omega)G_{nn}(\omega)}\,\ell_m(x)\ell_n(\xi) \tag{9}$$

Implied here is that all sources have identical directivity at a given frequency. Inclusion of the path lengths $\ell_m(x)$ and $\ell_n(\xi)$ makes Θ_{mn} a universal parameter, for a given jet, independent of microphone distances, provided that the microphones are in the acoustic far field. This formulation naturally brings out on the left-hand side of Eq. (7) the *complex coherence* of the pressure field,

$$\gamma_{mn}(\omega) \equiv \frac{G_{mn}(\omega)}{\sqrt{G_{mm}(\omega)G_{nn}(\omega)}} \tag{10}$$

Eq. (7) thus takes the form

$$\gamma_{mn}(\omega) = \int_{\mathcal{L}} \mathrm{e}^{\mathrm{i}\omega[\tau_m(x)-\tau_n(x)]}\psi(x,\omega)\,\mathrm{d}x \tag{11}$$

Eq. (11) serves as the definition of the coherence-based source distribution $\psi(x,\omega)$. The normalization of the cross-spectral density according to Eq. (10) was proposed by Fisher et al. [3] and Glegg [4] to account for the directivity of jet noise in the implementation of the polar correlation technique. The diagonal terms of Eq. (11) satisfy

$$1 = \int_{\mathcal{L}} \psi(x,\omega)\,\mathrm{d}x \tag{12}$$

Once the coherence-based noise source distribution has been obtained, the spectrum-based source distribution is calculated from

$$\Psi(x,\omega,\theta_m) = \psi(x,\omega)\Theta_{mm}(x,x,\omega) = \psi(x,\omega)G_{mm}(\omega)\ell_m^2(x). \tag{13}$$

For a given array position, Eq. (13) provides the noise source distribution corresponding to each microphone polar angle θ_m. It is evident from Eqs. (12) and (13) that axial integration of $\Psi(x,\omega,\theta_m)/\ell_m(x)^2$ gives the auto-spectrum $G_{mm}(\omega)$:

$$\int_{\mathcal{L}} \frac{1}{\ell_m(x)^2} \Psi(x,\omega,\theta_m)\,\mathrm{d}x = G_{mm}(\omega)\int_{\mathcal{L}} \psi(x,\omega)\,\mathrm{d}x = G_{mm}(\omega)$$

Therefore we have the desired self-consistent formulation for the directional noise source.

For the analysis that follows, it is convenient to introduce the array *response matrix*

$$\mathrm{T}_{mn}(x_0,\omega) = \mathrm{e}^{\mathrm{i}\omega[\tau_m(x_0)-\tau_n(x_0)]} \tag{14}$$

It describes the modeled coherence of the acoustic field for a point source at $x=x_0$ (i.e., for $\psi(x) = \delta(x-x_0)$). Eq. (11) then takes the form

$$\gamma_{mn}(\omega) = \int_{\mathcal{L}} \mathrm{T}_{mn}(x,\omega)\psi(x,\omega)\,\mathrm{d}x \tag{15}$$

3. Methods for noise source imaging

In this section we discuss three methods for imaging the noise source: delay-and-sum beamforming based on the complex coherence (rather than the cross-spectrum) of the acoustic field; deconvolution of the beamformer output; and direct spectral estimation using a minimization algorithm. The latter method obviates delay-and-sum beamforming.

3.1. Coherence-based beamforming

In delay-and-sum beamforming, the array output is [14]

$$\Phi(x,\omega) = \sum_{m=1}^{M}\sum_{n=1}^{M} W_m W_n \mathrm{e}^{\mathrm{i}\omega[\tau_n(x)-\tau_m(x)]} G_{mn}(\omega) \tag{16}$$

The microphone weights, W_m, are user-specified functions of ω and x. On selecting

$$W_m = \frac{w_m(x,\omega)}{\sqrt{G_{mm}(\omega)}}$$

and recognizing that the exponential term (steering matrix) is the complex transpose of the response matrix, Eq. (14), we obtain the coherence-based beamforming output:

$$\Phi(x,\omega) = \sum_{m=1}^{M}\sum_{n=1}^{M} w_m w_n \mathrm{T}^*_{mn}(x,\omega)\gamma_{mn}(\omega) \tag{17}$$

Expressing the coherence in terms of the source distribution, Eq. (15),

$$\Phi(x,\omega) = \int_{\mathcal{L}} \sum_{m=1}^{M}\sum_{n=1}^{M} w_m w_n \mathrm{T}_{mn}(\xi,\omega)\mathrm{T}^*_{mn}(x,\omega)\psi(\xi,\omega)\,\mathrm{d}\xi \tag{18}$$

On defining the point spread function (PSF) as

$$V(x,\xi,\omega) = \sum_{m=1}^{M}\sum_{n=1}^{M} w_m w_n \mathrm{T}_{mn}(\xi,\omega)\mathrm{T}^*_{mn}(x,\omega) \tag{19}$$

the coherence-based beamforming output becomes

$$\Phi(x,\omega) = \int_{\mathcal{L}} \psi(\xi,\omega)V(x,\xi,\omega)\,\mathrm{d}\xi \tag{20}$$

Eq. (20) shows that the array output is the convolution of the noise source distribution with the PSF. The PSF is not translation-invariant ($V(x,\xi,\omega) \neq V(x-\xi,\omega)$), so care is needed to prevent spatial distortions of the apparent noise source because of the spatial dependence of the PSF. This is possible to first order by preserving the integral under the main lobe of the PSF. This integral is approximated here as the beam width $b(x,\omega)$ times the height of the PSF:

$$I_{\mathrm{ML}} = \int_{\text{main lobe}} V(x,\xi,\omega)\,\mathrm{d}\xi \sim b(x,\omega)V(x,x,\omega) = D \tag{21}$$

where D is the jet diameter or any other characteristic length scale. From Eq. (19),

$$V(x,x,\omega) = \sum_{m=1}^{M}\sum_{n=1}^{M} w_m w_n \tag{22}$$

Therefore, the weights must satisfy

$$w_m(x,\omega) = \overline{w}_m \sqrt{\frac{D}{b(x,\omega)}} \tag{23}$$

where $\overline{w}_m$ are weight coefficients that satisfy $\sum \overline{w}_m = 1$. The beamwidth $b(x,\omega)$ can be estimated analytically or computed numerically from Eq. (19).

3.2. Deconvolution

Now we attempt to invert Eq. (20) and extract the coherence-based source distribution $\psi(x,\omega)$. From a mathematical standpoint, the weights w_m are immaterial to this process as they cancel from both sides of Eq. (20). However, assigning weights of special forms may aid in the numerical implementation of the inversion process. For simplicity we set $w_m=1$, in which case the beamforming output, Eq. (17), becomes

$$\Phi(x,\omega) = \sum_{m=1}^{M}\sum_{n=1}^{M} \mathrm{T}^*_{mn}(x,\omega)\gamma_{mn}(\omega) \tag{24}$$

and the PSF is

$$V(x,\xi,\omega) = \sum_{m=1}^{M}\sum_{n=1}^{M} \mathrm{T}_{mn}(\xi,\omega)\mathrm{T}^*_{mn}(x,\omega) \tag{25}$$

For a given frequency, the integral of Eq. (20) can be expressed as a summation over a finite number of sources K. Applying the discretizations

$$\Phi(x,\omega) \to \Phi_i$$

$$V(x,\xi,\omega) \to V_{ki}$$

$$\psi(\xi,\omega)\Delta\xi \to \psi_k$$

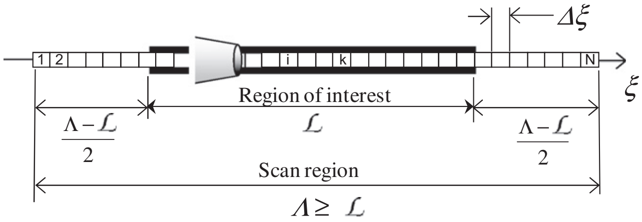

Fig. 3. Scan region and region of interest for deconvolution algorithm.

we obtain the linear system

$$\Phi_i = \sum_{k=1}^{K} V_{ik}\psi_k \tag{26}$$

The solution procedure generally follows the DAMAS approach of Brooks and Humphreys [14]. One distinction, however, is that we use the Bayesian-based Richardson–Lucy inversion algorithm [21,22] which has found wide application in image restoration. In the Richardson–Lucy method the point spread function $V(x,\xi)$ is assigned the meaning of a conditional probability $V(x|\xi)$ and the inversion relies on computing the inverse conditional probability $V(\xi|x)$. The advantage of Richardson–Lucy over Gauss–Seidel, used in DAMAS, is that its output is inherently non-negative and does not depend on the sequence of the equations. The iteration algorithm is

$$\psi_k^{(j)} = \psi_k^{(j-1)} \frac{1}{\sum_{i=1}^{K} V_{ik}} \sum_{i=1}^{K} \frac{V_{ik}\Phi_i}{\tilde{\Phi}_i}$$

$$\tilde{\Phi}_i = \sum_{k=1}^{K} V_{ik}\psi_k^{(j-1)} \tag{27}$$

The spatial extent of the region investigated and the resolution of grid points are critical parameters for the success of the deconvolution scheme. Important guidance comes from the deconvolution work of Brooks and Humphreys [14]. As shown in Fig. 3, the investigation domain consists of two overlapping regions: the scan region over which Eq. (27) is applied and the region of interest that includes the relevant noise sources. The scan region is larger than or equal to the region of interest. The length of the scan region Λ should be greater than the beam width and was selected to be $\Lambda = 2b$. For the present array it was determined that $b \approx 2\lambda$, therefore $\Lambda = 4\lambda$. The region of interest was chosen as $-5D < x < 25D$. The scan region was arranged symmetrically over the region of interest, as shown in Fig. 3. The spatial resolution should be a fraction of the wavelength and was set at $\Delta\xi = 0.25\lambda$. However, at low frequencies where the wavelength is very large, the resolution was set at $\Delta\xi = 0.01\mathcal{L}$. The combined scheme for the resolution was

$$\Delta\xi = \min(0.01\mathcal{L}, 0.25\lambda)$$

Typically, the method converged to a residual of 0.05 or less in 50 iterations, with slow improvement thereafter. The number of iterations was set at 100.

3.3. *Direct spectral estimation*

An alternative to beamforming followed by deconvolution is the direct estimation of the source distribution from Eq. (15)

$$\gamma_{mn}(\omega) = \int_{\mathcal{L}} \mathrm{T}_{mn}(x,\omega)\psi(x,\omega)\,\mathrm{d}x$$

The left- and right-hand sides represent the measured and modeled coherence matrices, respectively. We seek a source distribution $\psi(x,\omega)$ that minimizes the error between these two matrices. Here we do not manipulate the phase of each signal to steer the array in a particular direction. Instead, for each frequency, we minimize the errors between the independent elements of the measured and modeled coherence matrices. Similar inversion approaches for the polar correlation technique have been proposed by Tester et al. [5] and Fisher and Holland [6].

For M microphones, Eq. (15) contains $(M^2-M)/2$ distinct off-diagonal elements and one distinct diagonal element. The off-diagonal elements contain real and imaginary parts, rendering the total number of independent values to be minimized

$$J = M^2 - M + 1$$

which equals 57 for M=8. Letting j be the index of the distinct real and imaginary values of γ_{mn}, we write Eq. (15) as follows:

$$\gamma_j(\omega) = \int_{\mathcal{L}} \psi(x,\omega) T_j(x,\omega)\,\mathrm{d}x \tag{28}$$

Upon the discretizations

$$\psi(x,\omega)\delta x \to \psi_k$$

$$T_j(x,\omega) \to T_{jk}$$

we have the following linear system for each frequency:

$$\gamma_j = \sum_{k=1}^{K} \psi_k T_{jk} \tag{29}$$

To proceed further we adopt the approach Blacodon and Elias [23] who addressed a similar situation with airframe noise sources. Given that negative sources are not physical, a non-negative constraint is added by expressing the sources as

$$\psi_k = a_k^2$$

This leads to the least-squares unconstrained minimization of the function

$$F(a_k) = \sum_{j=1}^{J} \left| \gamma_j - \sum_{k=1}^{K} a_k^2 T_{jk} \right|^2 \tag{30}$$

The minimization is done iteratively using the restarted conjugate-gradient method of Shanno and Phua [24]. The number of noise sources K is generally arbitrary and does not need to match the number of independent equations J. However, the best results were obtained with $K \approx J$. For the results in this paper, $K=J=57$, and the sources were obtained on a fixed x-vector for all frequencies. The error was quantified in terms of $\sqrt{F/||\gamma_j||}$ and was around 0.2. The error in the diagonal terms was much smaller and around 0.05.

From Eqs. (19) and (20) we recognize that the deconvolution integral amounts to the Frobenius inner product of the direct spectral estimation relation, Eq. (15), with the steering matrix $T^*_{mn}(x,\omega)$. In fact, one could generalize the deconvolution problem by taking the inner product of Eq. (15) with any suitable matrix that would facilitate the inversion.

The direct spectral estimation method is computationally more expensive than the deconvolution because the conjugate-gradient method searches in K directions to minimize the gradient. Typically the routine required about 20 function calls for the gradient to be minimized. On the other hand, the method is attractive because its directness and simple formulation will facilitate the incorporation of more advanced models for the noise source (e.g., sources with finite coherence length scales).

4. Experimental setup

4.1. Flow facility

Experiments were conducted in UCI's Jet Aeroacoustics Facility, described in earlier publications [18]. The facility was operated in single-stream mode with pure air, at ambient reservoir temperature, supplied to a convergent round nozzle with exit diameter D=21.8 mm. The nozzle pressure ratio was 1.69 resulting in exit Mach number of 0.9 and exit velocity U=287 m/s. The jet Reynolds number was 5×10^5. In addition to the jet flow, a "point source" was obtained by four small (1.6 mm diameter) impinging jets in an arrangement similar to that used by Gerhold and Clark [19]. The impinging jets were supplied at a pressure ratio of 2.3. The resulting sound field had a moderate directivity, with the OASPL peaking at $\theta = 90^\circ$ and falling off by 3 dB for $\theta = 90^\circ \pm 30^\circ$.

4.2. Microphone array

The microphone phased array consists of eight 3.2 mm condenser microphones (Brüel & Kjær Model 4138) arranged on a circular arc centered at the vicinity of the nozzle exit. Fig. 4 shows the array geometry. The polar aperture of the array was 30° and the array radius was 1 m. The choice of the 30° polar aperture represents a compromise between small angular extent needed to resolve disparate noise sources and large angular extent required to maintain reasonable spatial resolution. Even though spatial resolution improves with deconvolution, one cannot expect deconvolution to succeed if the resolution of the image to be restored is severely degraded. The microphones were mounted on an arc-shaped holder and their angular spacing was logarithmic, starting from 2° for microphones 1 and 2 and ending with 10° for microphones 7 and 8. Uneven microphone spacing was used to mitigate the effects of spatial aliasing. The entire array structure was rotated around its center to place the array at the desired observation angle. Positioning of the array was done remotely using a stepper motor. An electronic inclinometer displayed the position of first microphone. The distances between the centers of the microphone protective grids were measured with accuracy of 0.1 mm using a digital caliper. A geometric calibration procedure provided the radial position of the array relative to the nozzle exit with accuracy of 2 mm.

The arrangement of the microphones inside the anechoic chamber, and the principal electronic components, is shown in Fig. 4. The microphones were connected, in groups of four, to two amplifier/signal conditioners (Brüel & Kjær Nexus 2690-A-OS4) with low-pass filter set at 300 Hz and high-pass filter set at 100 kHz. The four-channel output of each amplifier was sampled at 250 kHz per channel by a multi-function data acquisition board (National Instruments PCI-6070E). Two such

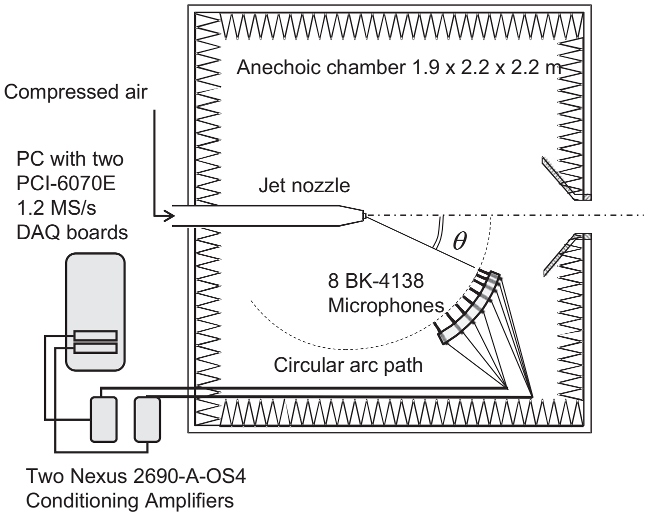

Fig. 4. Primary components of microphone array system.

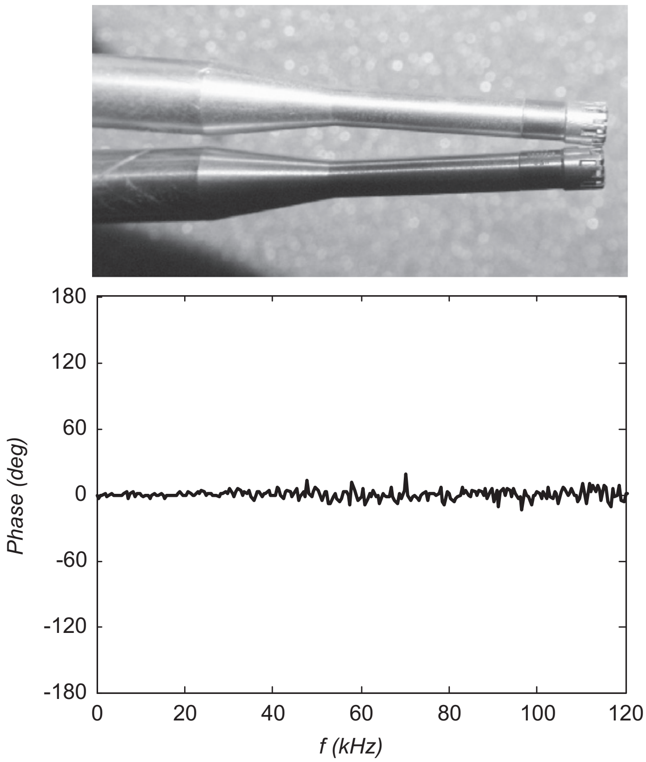

Fig. 5. Phase calibration.

boards, one for each amplifier, were installed in a Pentium 4 personal computer. National Instruments LabView software was used to acquire the signals. Time delays due to multiplexing in the data acquisition boards were measured by feeding the same signal to all the channels. These delays were compensated for in the source imaging algorithms.

Phase calibration for each microphone entailed placing the microphone against a reference microphone, ensuring perfect symmetry of the cartridge placement as illustrated in Fig. 5. The combination of the two microphones was placed at normal incidence to the far-acoustic field of the Mach 0.9 jet. The cross-spectral density between the two microphones was computed and its phase was plotted versus frequency. Fig. 5 shows a typical phase plot. It is seen that the relative phase is practically zero for all measured frequencies, indicating that there were no significant phase calibration errors.

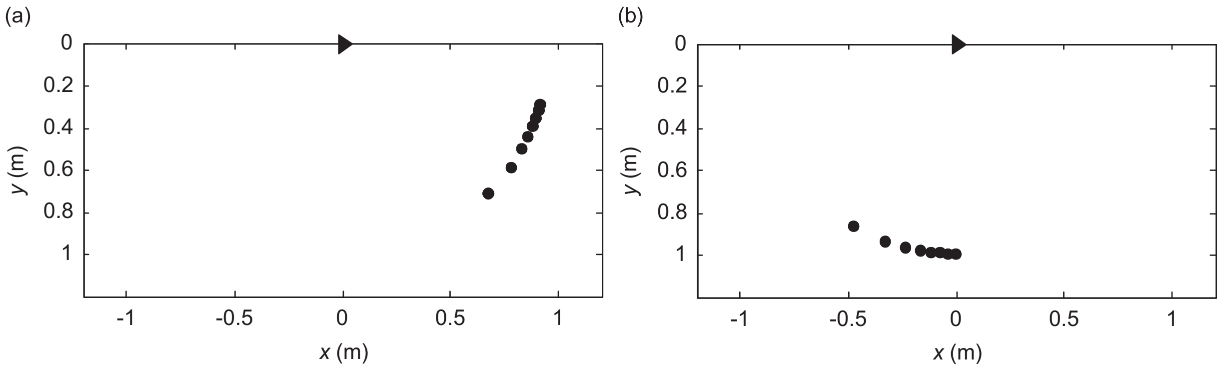

Fig. 6. Two positions of array: (a) $\theta_a = 30^\circ$; (b) $\theta_a = 105^\circ$. Triangles indicate nozzle exit.

The array observation angle is defined as $\theta_a = (\theta_1 + \theta_8)/2$. This paper discusses results obtained at two array observation angles: $\theta_a = 30^\circ$ and 105°. The placement of the microphones for each observation angle is plotted in Fig. 6.

4.3. Data processing

The computation of the cross-spectrum matrix, Eq. (4), involved the following steps. Each microphone signal consisted of $N_s=2^{18}=262\,144$ samples acquired at a sampling rate $F_s=250$ kHz. The maximum resolvable (Nyquist) frequency was $F_s/2=125$ kHz, although the high-pass filter was set a little lower at $f=100$ kHz. The size of the fast Fourier transform was $N_{\mathrm{FFT}} = 2048$ yielding a frequency resolution of 122 Hz. Each signal was divided into $K=64$ blocks of 4096 samples each, and the data within each block was windowed using a Hamming window. The cross-spectrum matrix G^k_{mn} for block k was computed using Fortran routines for auto-spectra and cross-spectra. The total cross-spectrum matrix was obtained from

$$G_{mn}(f) = \frac{1}{KW_h}\sum_{k=1}^{K} G^k_{mn}(f) \tag{31}$$

where W_h is a weighting constant for the Hamming window. Since the cross-spectrum matrix is Hermitian, only the diagonal and upper-triangle elements were computed; the lower-triangle elements were calculated as complex conjugates of the upper-triangle elements.

In calculating the spectrum-based source distribution, Eq. (13), the raw auto-spectrum $G_{mm_{\mathrm{raw}}}$ undergoes corrections to render it in lossless form. These corrections are performed in units of decibels:

$$10\log_{10}[G_{mm}(\omega)] = 10\log_{10}[G_{mm_{\mathrm{raw}}}(\omega)] + 93.98 - C_{\mathrm{fr}}(f) - C_{\mathrm{ff}}(f) + \alpha(f)R_m \tag{32}$$

The constant 93.98 comes from the normalization of the pressure by the reference pressure of 20 μPa, that is, $-20\log_{10}(20\times10^{-6}) = 93.98$. C_{fr} and C_{ff} are the corrections for the actuator response and free-field response, respectively; they are based on data provided by the manufacturer of the microphones. α is the atmospheric absorption coefficient (dB/m), computed using the formulas proposed by Bass et al. [20] for the measured values of relative humidity and temperature of the ambient air.

5. Results

5.1. Point sources

We first evaluate the performance of the inversion schemes for synthetic and physical point sources. The synthetic source is effectively a Dirac delta function placed at $\xi = x_s$. Eqs. (15) and (20) take, respectively, the forms

$$\mathrm{T}_{mn}(x_s,\omega) = \int_{\mathcal{L}} \mathrm{T}_{mn}(x,\omega)\psi(x,\omega)\,\mathrm{d}x$$

and

$$V(x,x_s,\omega) = \int_{\mathcal{L}} \psi(\xi,\omega)V(x,\xi,\omega)\,\mathrm{d}\xi$$

Their inversion should yield

$$\psi(\xi,\omega) = \delta(\xi - x_s)$$

The physical point source was created by the impinging jets described in Section 4.1, and was imaged with the microphone array at position $\theta_a = 105^\circ$ (Fig. 6b). Both the synthetic and physical point sources were located at $x_s=0$. In Fig. 7 we plot the

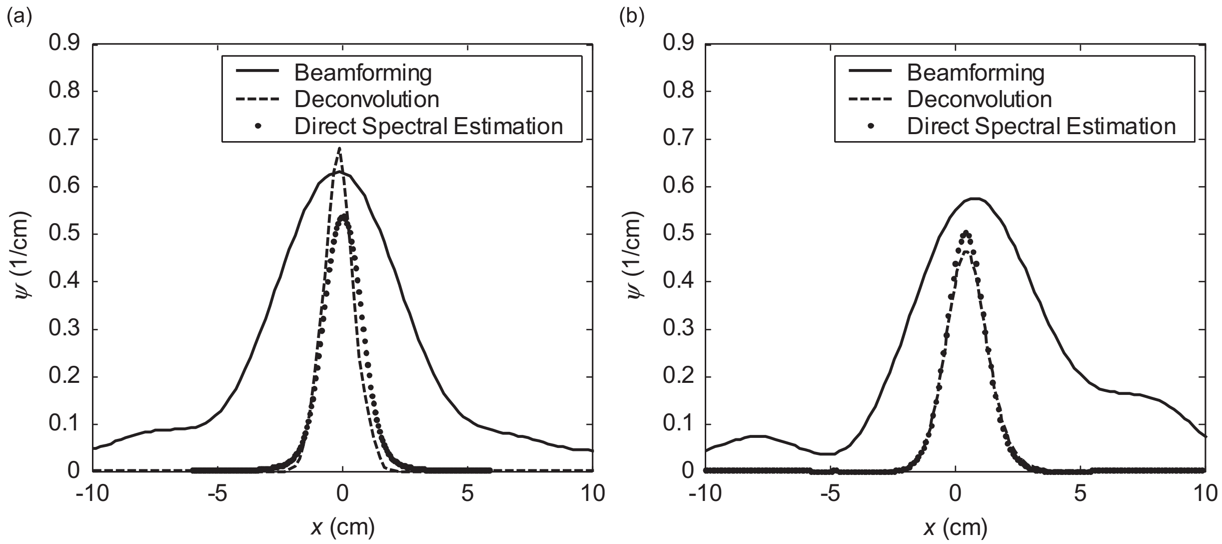

Fig. 7. Array output at f=10 kHz for: (a) synthetic point source; (b) impinging-jet source.

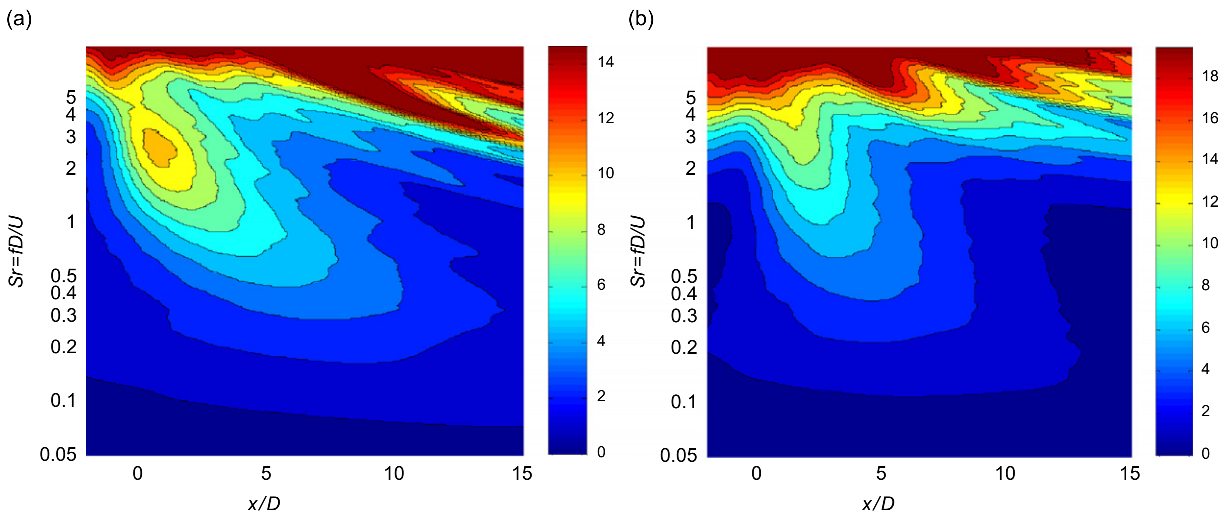

Fig. 8. Coherence-based beamforming output (linear scale). (a) $\theta_a=30^\circ$; (b) $\theta_a=105^\circ$.

axial distribution of the coherence-based source distribution, $\psi(x)$, at f=10 kHz ($Sr=0.77$), for the synthetic and physical point sources. We examine the outputs of the delay-and-sum beamformer, the deconvolution, and the direct spectral estimation. The deconvolution and direct spectral estimation techniques yield a five-fold improvement in spatial resolution compared to the delay-and-sum beamformer. The results are similar for the synthetic and physical point sources; small deviations in the beamforming output for the latter source arise from its finite volume and weak directivity.

5.2. Jet sources

We start with presentation of maps of the coherence-based source distributions $\psi(x,\omega)$ as viewed from the two array positions of Fig. 6. Fig. 8 shows the source distributions based on delay-and-sum beamforming. The noise maps are subject to blurring and distortions from the point spread function. It will be seen that the differences in the source maps at $\theta_a=30^\circ$ and 105° are due mainly to the variance in PSF between the two angles.

Fig. 9 shows the corresponding source maps after Richardson–Lucy deconvolution. The results are now much clearer and confined, and do not show major differences between the two array angles. The results of the direct spectral estimation are shown in Fig. 10. They agree well with the results obtained by the Richardson–Lucy deconvolution in Fig. 9. This is expected because, as mentioned earlier, the deconvolution integral amounts to the inner product of the direct spectral estimation

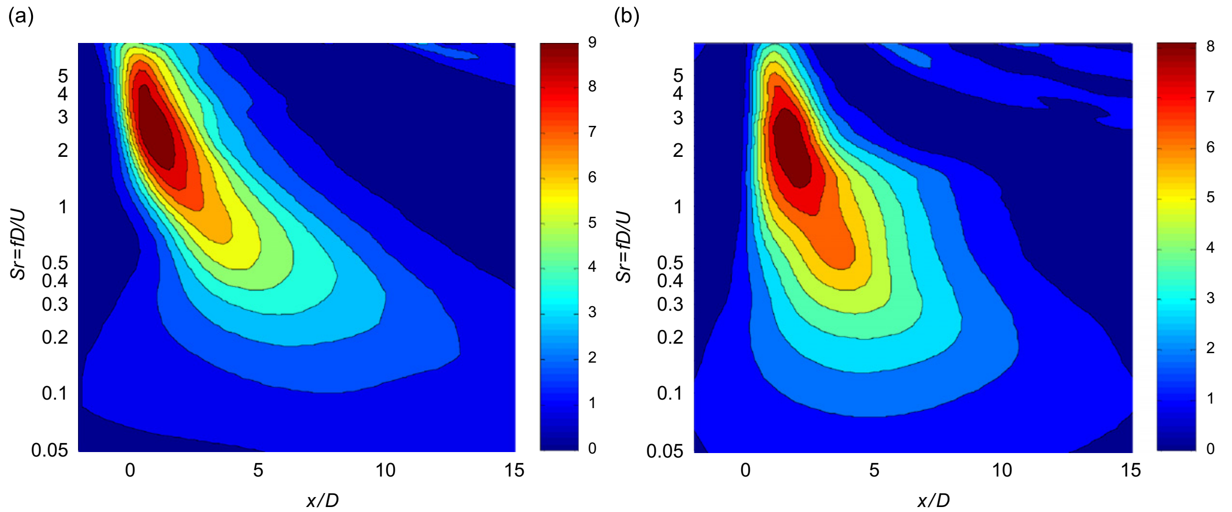

Fig. 9. Coherence-based source distribution after deconvolution of beamforming output (linear scale). (a) $\theta_a = 30^\circ$; (b) $\theta_a = 105^\circ$.

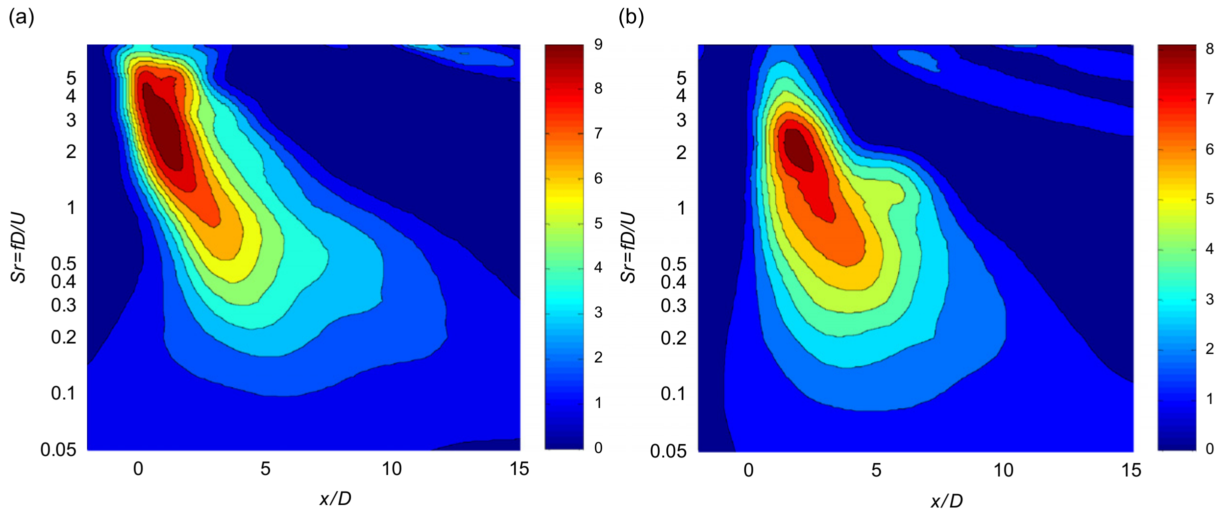

Fig. 10. Coherence-based source distribution obtained by direct spectral estimation (linear scale). (a) $\theta_a = 30^\circ$; (b) $\theta_a = 105^\circ$.

relation with the array steering matrix. Nevertheless, the similarity in the results of the two methods inspires confidence that both methods are producing reasonable noise source maps.

For both the deconvolution and direct spectral estimation methods, the noise source maps are clean up to about $Sr = 3$, above which weak "ghost" images appear. The appearance of ghost images is due to errors in the assumed positions of the microphone. At f=50 kHz, an error as small as 1 mm in the radial position of the microphone causes a 52° shift in the phase. Therefore, for $Sr > 3$ the levels in the main map start becoming inaccurate because the axial integration in Eq. (20) (deconvolution) or Eq. (15) (direct spectral estimation) includes the ghost images. The expectation is that the intensity of the noise sources should increase as their extent becomes smaller with increasing frequency.

Now we examine the spectrum-based source distribution, obtained from Eq. (13). Figs. 11 and 12 show contour maps of $\Psi(x,\omega)$ for microphone angles $\theta = 24^\circ$ and 105°, respectively. For each microphone angle, maps generated by the three techniques are shown on the same dynamics range. Values outside the dynamics range are plotted white. The beamformer output produces axially stretched images with significant sidelobes. The Richardson–Lucy deconvolution and direct spectral estimation techniques yield almost identical results, with substantial improvements in fidelity. Notable are the sharp cutoffs at x=0 for $Sr > 0.5$ and the absence of sidelobes. For both angles, the location of the strongest noise source occurs at $x/D \approx 5$, which corresponds to the region near the end of the primary potential core for this jet. The corresponding Strouhal numbers are Sr=0.2 for $\theta = 24^\circ$ and Sr=0.5 for $\theta = 105^\circ$. For all maps, the location of peak noise moves toward the nozzle exit as the frequency increases.

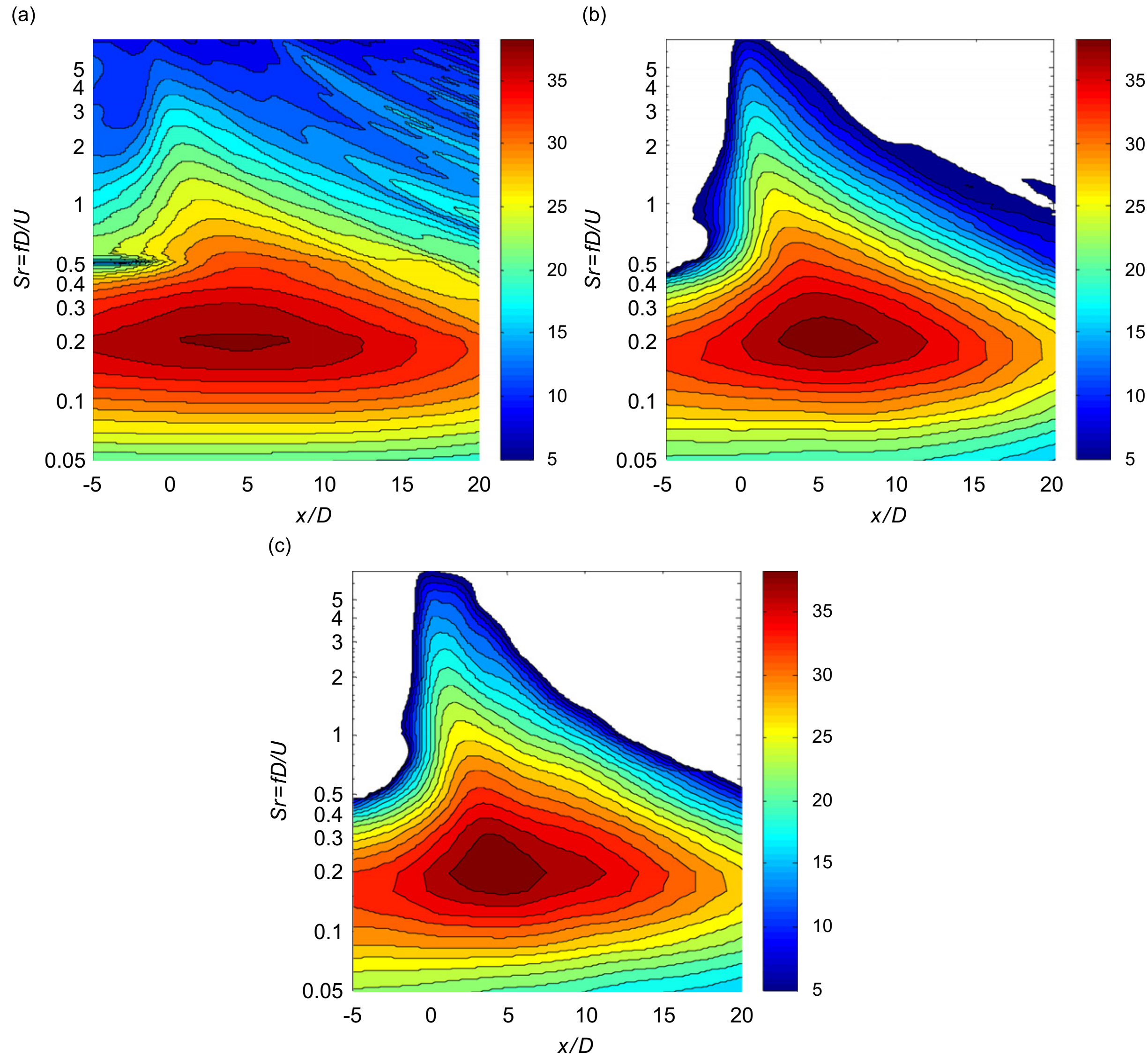

Fig. 11. Spectrum-based source distribution for $\theta = 24^\circ$ (decibels). (a) Beamforming; (b) RL deconvolution; (c) direct spectral estimation.

5.3. Spatial coherence of acoustic field

The results of Figs. 9 and 10 show a strong similarity between noise sources emitting at small and large angles relative to the jet axis. Here we investigate how this finding may affect the polar coherence of the far-acoustic field. Past studies that measured the coherence of the acoustic field, for example Tam et al. [17], noted strong polar coherence for noise emitted in the direction of peak emission and weak polar coherence for noise emitted at large angles. Although this appears consistent with the potentially disparate noise sources discussed in Introduction, interpretation of the spatial coherence of the acoustic field must take into account geometric path length effects inherent to the design of the instrument that images the noise sources, in this case the microphone array.

The response of the microphone array is a function of the arrangement of the microphones and of the assumed model for the acoustic source. For the spatially incoherent source model described in Section 2, the response of the array is given by Eq. (14). In terms of the path lengths ℓ, it takes the form

$$\mathrm{T}_{mn}(x,\omega) = \mathrm{e}^{\mathrm{i}(\omega/a)[\ell_m(x)-\ell_n(x)]}.$$

Consider the polar microphone arrangement of Fig. 13. From the geometry,

$$\ell_m(x)^2 = R^2 - 2Rx\cos\theta_m + x^2$$

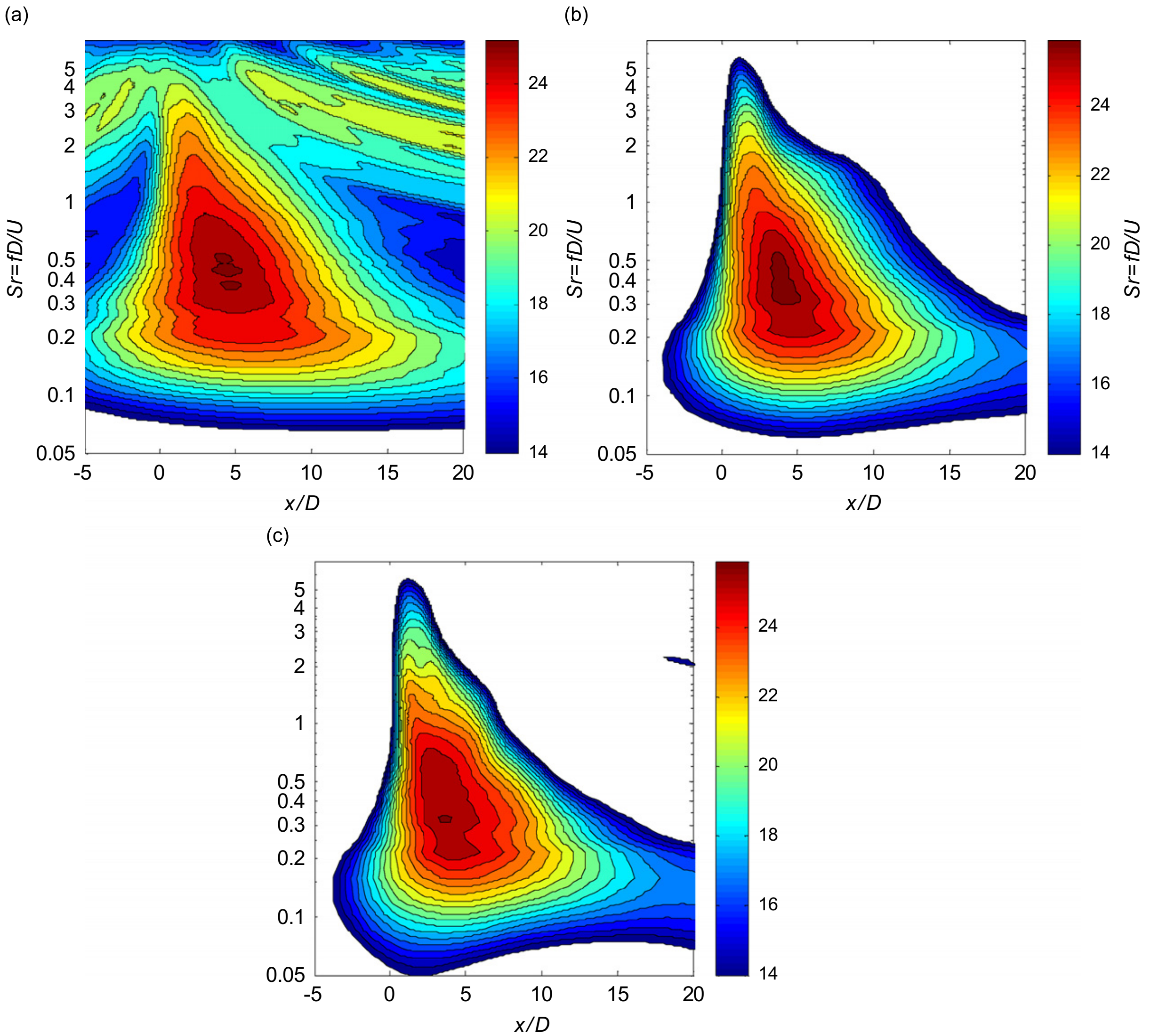

Fig. 12. Spectrum-based source distribution for $\theta=105^\circ$ (decibels). (a) Beamforming; (b) RL deconvolution; (c) direct spectral estimation.

For $R \gg x$, we can make the following approximation:

$$\ell_m(x)-\ell_n(x)=\frac{\ell_m(x)^2-\ell_n(x)^2}{\ell_n(x)+\ell_m(x)} \approx \frac{2Rx(\cos\theta_n-\cos\theta_m)}{2R}=x(\cos\theta_n-\cos\theta_m)$$

The last term brings out the angular response of the polar array:

$$\mu_{mn}=\cos\theta_n-\cos\theta_m=2\sin\left(\frac{\theta_m-\theta_n}{2}\right)\sin\left(\frac{\theta_m+\theta_n}{2}\right) \tag{33}$$

We note that the response of the microphone array depends not only on the separation angle $\Delta\theta=\theta_n-\theta_m$ but also on the average angle $(\theta_m+\theta_n)/2$ of any pair of microphones. The latter term causes a slow response with $\Delta\theta$ at shallow polar angles and a fast response at polar angles near 90°. For a polar arrangement of microphones, therefore, Eq. (15) can be approximated as

$$\gamma_{mn}(\omega)=\int_{\mathcal{L}}\exp\left(i\frac{\omega x}{a}\mu_{mn}\right)\psi(x,\omega)\,\mathrm{d}x \tag{34}$$

If the source distribution $\psi(x,w)$ is similar at small and large observation angles, as Figs. 9 and 10 suggest, then the coherence $\gamma_{mn}(\omega)$ should collapse when plotted against the array angular response parameter μ_{mn}. Fig. 14 plots the coherence modulus $|\gamma_{mn}|$ versus angular separation $\theta_n-\theta_m$ and versus the array angular response parameter for array polar angles $\theta_a=30^\circ$ and 105°, and for Strouhal numbers Sr=1 and 3. All the non-trivial permutations of θ_m and θ_n are included. The coherence versus

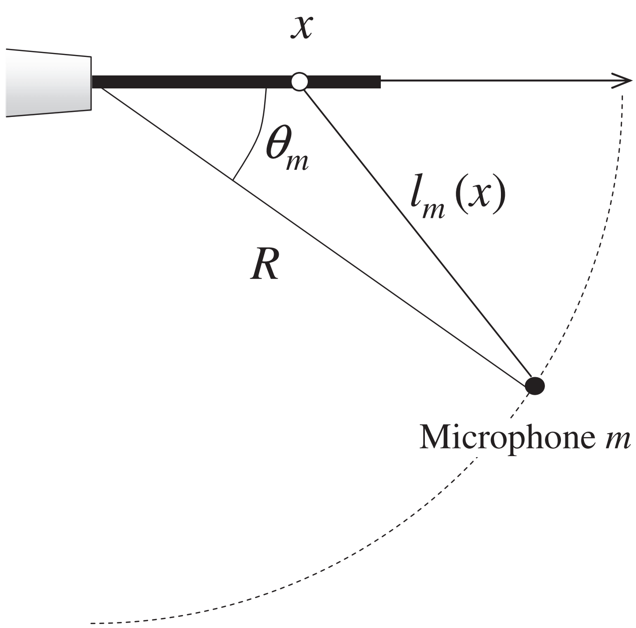

Fig. 13. Geometry of polar arrangement of microphones.

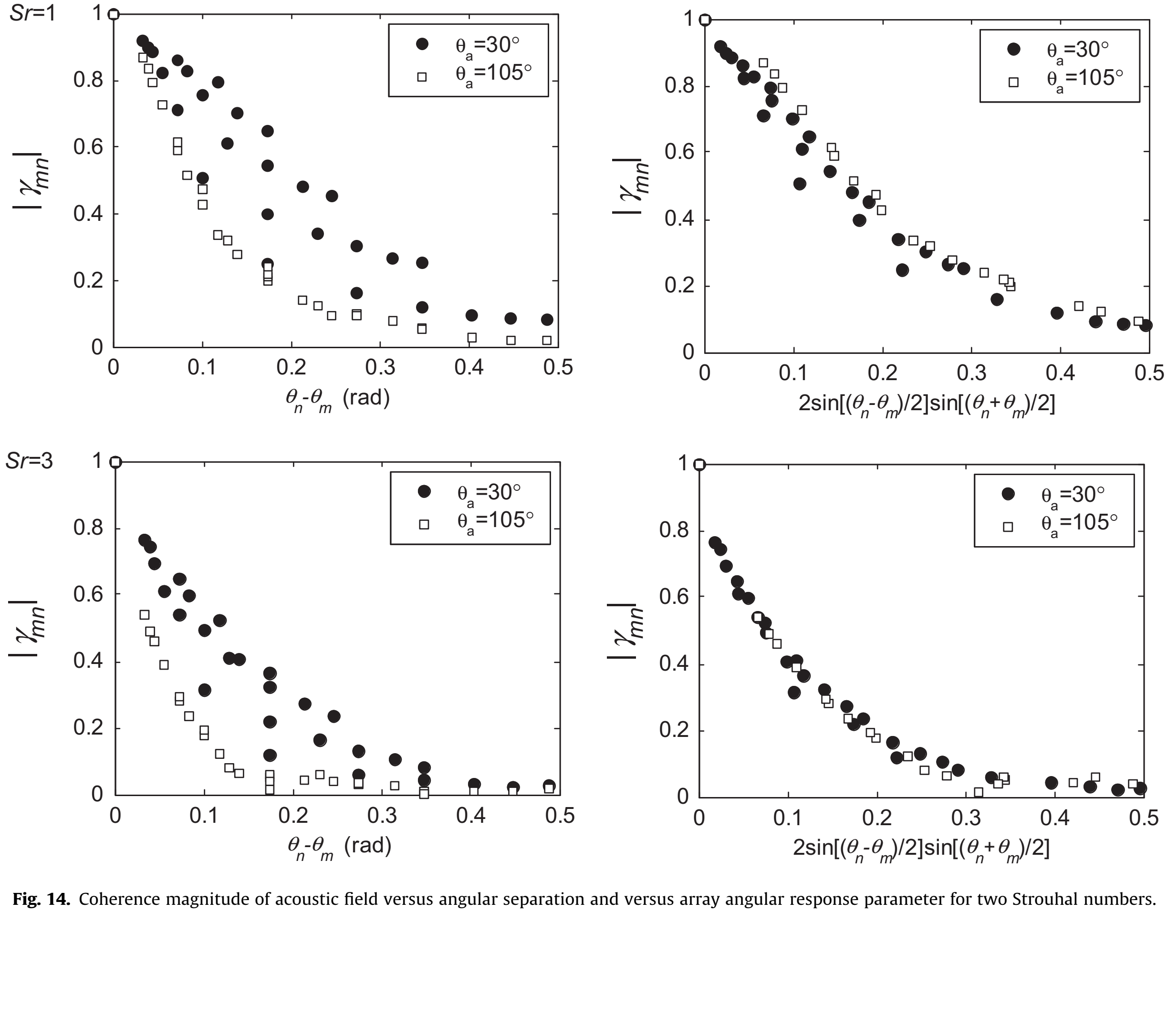

Fig. 14. Coherence magnitude of acoustic field versus angular separation and versus array angular response parameter for two Strouhal numbers.

angular separation plots replicate the trends seen by previous investigations [17], namely that the coherence decays rapidly with $\Delta\theta$ at large angles and slowly at shallow angles. However, when the coherence is plotted against the array angular response parameter the distributions for the two array observation angles practically collapse.

A correlation similar to that of Fig. 14 (right column) was performed by Fisher et al. [3] for their polar correlation data. They plotted the coherence magnitude and phase versus the parameter $\mu = \cos\theta_2 - \cos\theta_1$, which is the array angular response with two microphones (Eq. (33)), microphones 1 and 2 being the reference and traversable microphones, respectively. They observed a collapse of the coherence plots for small and large observation angles of the reference microphone. The reader is instructed to compare Fig. 14 of the present paper with Fig. 12 of Ref. [3]. The provisional conclusion of Ref. [3] was that the jet mixing noise source distributions are independent of observation angle. It is noteworthy that the present correlations, using multiple microphones and all their mutual coherences (i.e., there is no "reference" microphone), confirm this important finding of Ref. [3].

6. Conclusions

This study relates to the imaging of noise sources that are distributed and strongly directional, such as in turbulent jets. The goal is to generate high-resolution noise source maps with self-consistency, i.e., their integration over the extent of the noise source region gives the far-field pressure auto-spectrum for a particular emission direction. The jet noise source is modeled as an axial distribution of spatially incoherent point sources. For self-consistency, it is necessary to include a directivity matrix in the formulation of the source cross-spectral density. The resulting source distribution is based on the complex coherence, rather than the cross-spectrum, of the measured acoustic field.

Three coherence-based imaging methods were applied to a Mach 0.9 turbulent jet: delay-and-sum beamforming; deconvolution of the beamformer output, based on the Richardson–Lucy inversion; and direct spectral estimation that uses a conjugate-gradient method to minimize the difference between the measured and modeled coherences of the acoustic field. The jet was imaged at small and large angles relative to the downstream axis using an eight-microphone array with 30° angular aperture.

The delay-and-sum beamformer generates noise source maps with strong spatial distortions and sidelobes. Deconvolution leads to a five-fold improvement in spatial resolution and significantly reduces the intensity of the sidelobes. The direct spectral estimation produces maps very similar to those obtained by deconvolution. The two techniques are in fact related: the deconvolution integral amounts to the tensor inner product of the direct spectral estimation relation with the array response matrix. Although the direct spectral estimation is computationally more demanding than the deconvolution, its directness makes it an attractive tool for more complex noise source models.

The coherence-based noise source maps, obtained by deconvolution or direct spectral estimation, are similar at small and large observation angles relative to the jet axis. The apparent independence of the noise source distribution on observation angle is further supported by the collapse of the polar coherence of the acoustic field when plotted against the angular response parameter of the microphone array.

Acknowledgements

The author wishes to thank Dr. Robert Dougherty (Optinav, Inc.) for suggesting the Richardson–Lucy inversion method and Mr. Ali Dadvar for his assistance in the design and installation of the microphone array as a graduate student.

References

[1] F.-R. Grosche, Distribution of sound source intensities in subsonic and supersonic jets, AGARD CP-131, Paper 4, 1974.
[2] J. Laufer, R. Schlinker, R.E. Kaplan, Experiments on supersonic jet noise, *AIAA Journal* 14 (4) (1976) 489–497.
[3] M.J. Fisher, M. Harper-Bourne, S.A.L. Glegg, Jet engine source location: the polar correlation technique, *Journal of Sound and Vibration* 51 (1) (1977) 23–54.
[4] S.A.L. Glegg, The accuracy of source distributions measured by using polar correlation, *Journal of Sound and Vibration* 80 (1) (1982) 31–40.
[5] B.J. Tester, M.J. Fisher, Engine noise source breakdown: theory, simulation and results, AIAA Paper 1981-2040, 1981.
[6] M.J. Fisher, K.R. Holland, Measuring the relative strengths of a set of partially coherent acoustic sources, *Journal of Sound and Vibration* 102 (1) (1997) 103–125.
[7] J. Billingsley, R. Kinns, The acoustic telescope, *Journal of Sound and Vibration* 48 (4) (1976) 485–510.
[8] R.A. Gramann, J.W. Mocio, Aeroacoustic measurements in wind tunnels using adaptive beamforming methods, *Journal of the Acoustical Society of America* 97 (6) (1995) 3694–3701.
[9] M. Mosher, Phased arrays for aeroacoustic testing: theoretical development, AIAA Paper 1996-1713, 1996.
[10] W.M. Humphreys, T.F. Brooks, W.W. Hunter, K.R. Meadows, Design and use of microphone directional arrays for aeroacoustic measurements, AIAA Paper 1998-0471, 1998.
[11] S. Narayanan, T.J. Barber, D.R. Polak, High subsonic jet experiments: turbulence and noise generation studies, *AIAA Journal* 40 (3) (2002) 430–437.
[12] S.R. Venkatesh, D.R. Polak, S. Narayanan, Beamforming algorithm for distributed source localization and its application to jet noise, *AIAA Journal* 41 (7) (2003) 1238–1246.
[13] S.S. Lee, J. Bridges, Phased-array measurements of single flow hot jets, AIAA Paper 2005-2842, 2005.
[14] T.F. Brooks, W.M. Humphreys, A deconvolution approach for the mapping of acoustic sources determined from phased microphone arrays, *Journal of Sound and Vibration* 294 (4–5) (2006) 856–879.
[15] R.P. Dougherty, Extensions of DAMAS and benefits and limitations of deconvolution in beamforming, AIAA 2005-2961, 2005.
[16] C.K.W. Tam, Jet noise: since 1952, *Theoretical and Computational Fluid Dynamics* 10 (1998) 393–405.

[17] C.K.W. Tam, K. Viswanathan, K.K. Ahuja, J. Panda, The sources of jet noise experimental evidence, *Journal of Fluid Mechanics* 615 (2008) 253–292.
[18] D. Papamoschou, M. Debiasi, Directional suppression of noise from a high-speed jet, *AIAA Journal* 39 (3) (2001) 380–387.
[19] C.H. Gerhold, L.R. Clark, M.H. Dunn, J. Tweed, Investigation of acoustical shielding by a wedge-shaped airframe, *Journal of Sound and Vibration* 294 (1–2) (2006) 49–63.
[20] H.E. Bass, L.C. Sutherland, D.T. Blackstock, D.M. Hester, Atmospheric absorption of sound: further developments, *Journal of the Acoustical Society of America* 97 (1) (1995) 680–683.
[21] W.H. Richardson, Bayesian-based iterative method of image restoration, *Journal of the Optical Society of America* 62 (1) (1972) 55–59.
[22] L.B. Lucy, Iterative technique for rectification of observed distribution, *Astronomical Journal* 79 (6) (1964) 745–754.
[23] D. Blacodon, G. Elias, Level estimation of extended acoustic sources using a parametric method, *Journal of Aircraft* 41 (6) (2004) 1360–1369.
[24] D.F. Shanno, K.H. Phua, Minimization of unconstrained multivariate functions, *ACM Transactions on Mathematical Software* 6 (4) (1980) 618–622.